



Engineering of tissue inhibitor of metalloproteinases TIMP-1 for fine discrimination between closely related stromelysins MMP-3 and MMP-10

Received for publication, November 9, 2021, and in revised form, January 21, 2022. Published, Papers in Press, January 29, 2022.
<https://doi.org/10.1016/j.jbc.2022.101654>

Maryam Raeeszadeh-Sarmazdeh¹, Mathew Coban¹ , Shivansh Mahajan¹, Alexandra Hockla¹,
Banumathi Sankaran², Gregory P. Downey^{3,4}, Derek C. Radisky¹, and Evette S. Radisky^{1,*} 

From the ¹Department of Cancer Biology, Mayo Clinic Comprehensive Cancer Center, Jacksonville, Florida, USA; ²Division of Molecular Biophysics and Integrated Bioimaging, Berkeley Center for Structural Biology, Lawrence Berkeley National Laboratory, Berkeley, California, USA; ³Departments of Medicine, Pediatrics, and Immunology and Genomic Medicine, National Jewish Health, Denver, Colorado, USA; ⁴Departments of Medicine, and Immunology and Microbiology, University of Colorado Anschutz Medical Campus, Aurora, Colorado, USA

Edited by George DeMartino

Matrix metalloproteinases (MMPs) have long been known as key drivers in the development and progression of diseases, including cancer and neurodegenerative, cardiovascular, and many other inflammatory and degenerative diseases, making them attractive potential drug targets. Engineering selective inhibitors based upon tissue inhibitors of metalloproteinases (TIMPs), endogenous human proteins that tightly yet nonspecifically bind to the family of MMPs, represents a promising new avenue for therapeutic development. Here, we used a counter-selective screening strategy for directed evolution of yeast-displayed human TIMP-1 to obtain TIMP-1 variants highly selective for the inhibition of MMP-3 in preference over MMP-10. As MMP-3 and MMP-10 are the most similar MMPs in sequence, structure, and function, our results thus clearly demonstrate the capability for engineering full-length TIMP proteins to be highly selective MMP inhibitors. We show using protein crystal structures and models of MMP-3-selective TIMP-1 variants bound to MMP-3 and counter-target MMP-10 how structural alterations within the N-terminal and C-terminal TIMP-1 domains create new favorable and selective interactions with MMP-3 and disrupt unique interactions with MMP-10. While our MMP-3-selective inhibitors may be of interest for future investigation in diseases where this enzyme drives pathology, our platform and screening strategy can be employed for developing selective inhibitors of additional MMPs implicated as therapeutic targets in disease.

Matrix metalloproteinases (MMPs) are a family of zinc endopeptidases (23 in humans) with important functions in extracellular matrix remodeling and degradation and play

central roles in development of many human diseases, including cancer, pulmonary diseases, and neurological disorders (1–7). Several past efforts to develop efficient therapeutics against MMPs failed in the late stages of clinical trials, in part because of nonselective inhibition of many MMPs and related metalloproteinases (6, 8). Lack of selectivity was a critical issue because broad-spectrum metalloproteinase inhibition caused serious dose-limiting musculoskeletal toxicity, and in some cases, it proved to be counterproductive by inhibiting MMPs with protective roles in disease alongside those that drive pathology (9–11). Development of highly selective MMP inhibitors has been extremely challenging. However, new strategies for developing selective MMP inhibitors may lead to much-needed molecular probes for better defining individual MMP functions in biology and disease, and ultimately, to more effective therapeutics targeting the specific MMPs that are underlying causes of disease.

Protein engineering using directed evolution offers a robust method to define the sequence–structure–function relationships of proteins, and directed evolution was previously used to develop new proteins with novel desired properties based on the scaffolds of existing natural proteins (12, 13). MMPs are regulated *in vivo* by tissue inhibitors of metalloproteinases (TIMPs) (14), and although these natural proteins possess broad specificity for inhibition of many MMPs, we and others have demonstrated that their inhibitory spectrum can be altered through protein engineering using yeast surface display and directed evolution. Prior work has focused primarily on engineering the N-terminal domain of TIMPs, an independently folding and stable domain that retains MMP inhibitory capability (15, 16). Yeast surface display of the N-terminal domain of TIMP-2 was used successfully as a directed evolution platform to develop inhibitors of MMP-9 and MMP-14 with enhanced affinity and selectivity (17–20). Recently, we demonstrated that full-length TIMPs could offer further advantages as scaffolds for engineering inhibitors with improved binding toward target MMPs. Directed evolution of full-length TIMP-1, containing two domains that together form the

* For correspondence: Evette S. Radisky, radisky.evette@mayo.edu.
Present address for Maryam Raeeszadeh-Sarmazdeh: Department of Chemical and Materials Engineering, University of Nevada, Reno, Nevada 89557, USA.
Present address for Shivansh Mahajan: Division of Chemistry and Chemical Engineering, California Institute of Technology, Pasadena, California 91125, USA.

Engineering MMP-3-selective TIMP-1

MMP-binding interface, revealed that engineered mutations in its N-terminal and C-terminal domains could work synergistically to enhance binding affinity toward the target MMP-3 (21). Our previous study was designed to identify MMP-3 “ultrabinders,” which demonstrated up to 10-fold improved binding affinity compared with WT TIMP-1 and inhibited MMP-3 with equilibrium inhibition constant (K_i) values in the low picomolar range (21). In the present study, we focused on developing and evaluating the potential of our yeast surface display platform for evolving selective TIMP-1 variants capable of discriminating between very closely related MMPs.

Among all MMP catalytic domains, the stromelysins MMP-3 and MMP-10 are the most similar in sequence (85% identity), structure, and substrate specificity and thus offer a rigorous challenge of our strategy to develop highly selective TIMPs (22, 23). MMP-3 is also a notable therapeutic target. MMP-3 has a demonstrated role in tumorigenesis and tumor progression of breast, lung, and pancreatic cancers, in which it is a driver of epithelial to mesenchymal transition (24–28). It is also a therapeutic target in several other inflammatory and degenerative diseases, including rheumatoid arthritis, where MMP-3 levels in patient serum correlate with progressive joint damage (29), lung fibrosis, where MMP-3 is consistently upregulated in patients with idiopathic pulmonary fibrosis (IPF) and drives pathogenic fibrotic changes (30–32) and in the acute respiratory distress syndrome (ARDS) where elevated levels of MMP-3 correlate with high mortality (33–35). Here, we aimed to engineer TIMP variants capable of distinguishing between MMP-3 *versus* MMP-10 to provide insight into determinants of selective MMP binding and inhibition and as a demonstration of the power of our TIMP engineering platform. Using an innovative counter-selective strategy, we screened a TIMP-1 yeast surface display library using fluorescent-activated cell sorting (FACS) and identified variants that bind selectively to MMP-3 in the presence of incremental amounts of the competitor ligand MMP-10. TIMP-1 mutants isolated after five rounds of competitive screening revealed up to 23-fold improvement in binding selectivity toward MMP-3 *versus* MMP-10 compared to WT TIMP-1. DNA sequencing of TIMP-1 variants with improved MMP-3 binding selectivity revealed key residues that are responsible for improvements in selectivity. Protein crystal structures were solved of the two TIMP-1 variants showing greatest improvement in MMP-3 binding selectivity in complex with the target MMP-3, and comparison of these structures with models of complexes with the counter-target MMP-10 reveal the structural alterations responsible for the newly evolved selectivity.

Results

A counter-selective screening platform to isolate TIMP-1 variants with selective binding to MMP-3

We previously selected MMP-3 ultrabinders from a targeted library of human TIMP-1 mutants displayed on the yeast surface (21). Despite the significant improvement for MMP-3 binding affinity, these TIMP-1 variants were nonselective,

showing improvement in binding toward MMP-10 as well, relative to the WT TIMP-1 (Fig. S1). To enhance selectivity toward MMP-3 *versus* MMP-10, we next devised a counter-selective strategy to screen our naïve library of TIMP-1 mutants to identify binders selective for MMP-3 over MMP-10. This library of TIMP-1 variants incorporates targeted diversity at eight residues within the N-terminal domain and nine residues within the C-terminal domain that are concentrated at the MMP-binding interface, with an average of 3 to 4 mutations per variant (Fig. 1, A and B). In our counter-selective screening strategy, the yeast-displayed library of TIMP-1 mutants was screened for biotinylated MMP-3 catalytic domain (MMP-3cd) binding in the presence of unlabeled competitive binder MMP-10 catalytic domain (MMP-10cd). Bound MMP-3cd was detected with fluorophore-labeled streptavidin and protein display levels were quantified using fluorophore-conjugated anti-c-myc antibody followed by fluorescent-activated cell sorting (FACS) (Fig. 1C). The TIMP-1 library of targeted mutants went through rounds of competitive FACS screening while incrementally increasing the ratio of unlabeled MMP-10cd (competitive ligand) to biotinylated MMP-3cd (specific target), selecting for variants with enhanced selectivity toward MMP-3cd *versus* MMP-10cd. This approach excluded TIMP-1 variants with significant binding affinity toward MMP-10, since they would have disproportionately bound to the excess quantity of unlabeled MMP-10cd in preference to MMP-3cd and thus would have escaped detection and been eliminated during the increasingly stringent FACS screening rounds. After five rounds of counter-selective FACS, the population of selected TIMP-1 mutants showed dramatically improved binding selectivity toward MMP-3cd (up to 23-fold) compared with MMP-10cd, whereas WT TIMP-1 shows similar binding to MMP-3cd and MMP-10cd (Fig. 1D).

Individual TIMP-1 variants isolated using the counter-selective strategy showed significant enhancement of binding selectivity toward MMP-3cd versus MMP-10cd on the yeast surface

The TIMP-1 variants isolated after five rounds of counter-selective MMP-3cd *versus* MMP-10cd FACS screening were further individually analyzed *via* DNA sequencing to identify mutations compared with WT human TIMP-1. DNA sequencing analysis and alignments of the genes encoding the six most prevalent TIMP-1 variants in the selected pool revealed 4 to 5 mutations per clone located within the five interacting loops of TIMP-1, as expected per targeted library design (Fig. 2A). Among the TIMP-1 mutants analyzed by DNA sequencing of their genes, mutation L34G located in the AB loop and M66D/G/S and E67N/Y/H located in the C-connector loop were the most frequent mutations observed (Fig. 2A). The L34G mutation had been identified from the high-affinity MMP-3 variants that were isolated previously (21), suggesting that the L34G mutation has a key role in improving binding affinity of TIMP-1 toward MMP-3. Further quantitative measurement of expression on the yeast surface

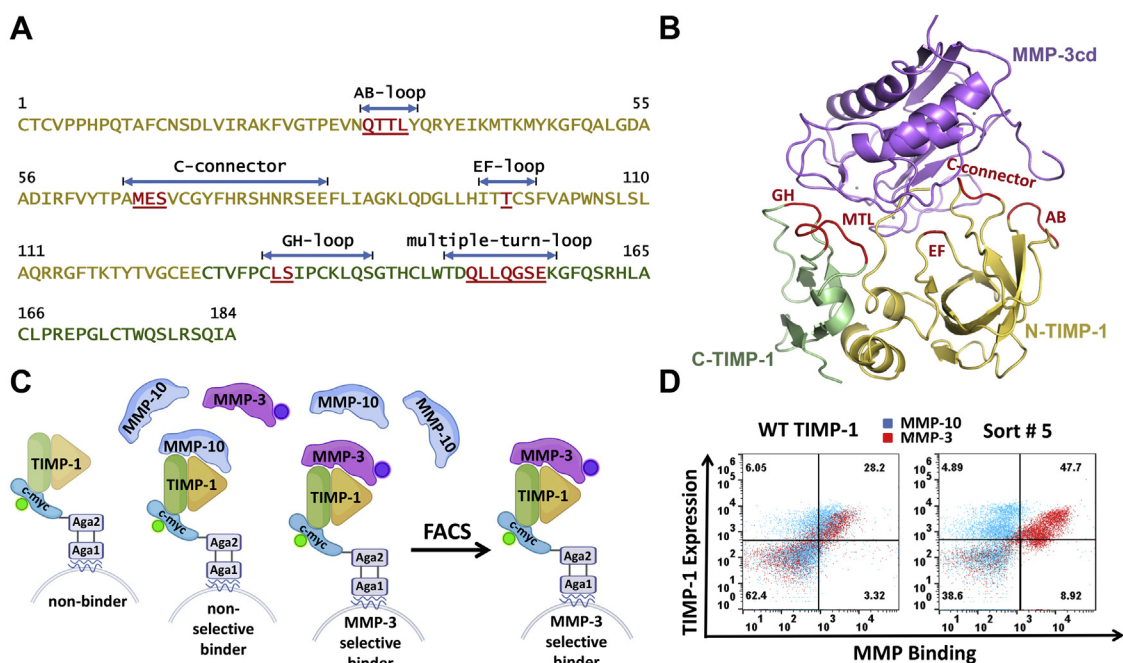


Figure 1. Counter-selective strategy for engineering TIMP-1 variants with high binding selectivity for MMP-3. *A*, WT TIMP-1 sequence is shown, with N-terminal domain residues in *gold* and C-terminal domain residues in *green*; MMP-interacting regions are annotated with *blue arrows* and the name of corresponding loops in *black*. Residues diversified in the targeted library in each interacting loop are shown in *red* and *underlined*. *B*, positions of diversified TIMP-1 loop regions are shown in *red* in the context of the MMP-3–TIMP-1 crystal structure, PDB ID: 1UEA. MMP-3 is colored *purple*, and the N-terminal and C-terminal domains of TIMP-1 are colored *gold* and *green*, respectively. *C*, schematic diagram illustrates yeast surface display screening strategy. TIMP-1 was genetically fused to the N terminus of Aga2p yeast surface protein via a linker containing the c-myc epitope tag. The yeast displayed library of TIMP-1 variants was screened for binding to biotinylated MMP-3cd in the presence of excess competitor ligand, unlabeled MMP-10cd. TIMP-1 expression was quantified by immunolabeling of the c-myc tag using Alexa Fluor 488-conjugated anti-cmyc antibody (*green sphere*); MMP-3 binding was quantified using Alexa Fluor 647-conjugated streptavidin (*purple sphere*). TIMP-1 variants with enhanced selectivity for MMP-3cd binding were isolated using FACS. *D*, flow cytometry dual scatter plots of TIMP-1 expression (*y-axis*) versus MMP-binding (*x-axis*) are shown for WT TIMP-1 (*left panel*) and the pool of TIMP-1 variants selected from the library after five rounds of FACS (*right panel*). MMP-3cd binding is shown in *red*, and MMP-10cd binding is shown in *blue*. FACS, fluorescence-activated cell sorting; MMP-3, matrix metalloproteinase 3; PDB, Protein Data Bank; TIMP-1, tissue inhibitor of metalloproteinases 1.

and binding to MMP-3cd and MMP-10cd were performed on these isolated TIMP-1 mutants using flow cytometry (Fig. 2B). Two of the selected TIMP-1 variant clones in particular, clone C4 (L34G/M66D/T98G/P131S/Q153N) and C6 (L34G/M66S/E67Y/L133N/S155L), showed the highest binding selectivity between MMP-3cd and MMP-10cd (Fig. 2B) and were thus selected for further study.

Soluble TIMP-1 variants isolated using the counter-selective strategy showed significant selectivity toward MMP-3 compared with MMP-10 and MMP-9 in MMP inhibition assays

The gene sequences for the most selective MMP-3cd binding variants (TIMP-1-C4 and TIMP-1-C6) were next subcloned and expressed to produce soluble purified proteins. The TIMP-1-C4 and TIMP-1-C6 soluble variant proteins were then evaluated for MMP-3cd, MMP-9cd, and MMP-10cd inhibition using a fluorometric substrate in the presence of increasing concentrations of the inhibitors (TIMP-1 variants). Fluorescence intensity values were fitted to Morrison's tight-binding equation to determine K_i (Fig. 3 and Table 1).

We found up to an order of magnitude improvement for MMP-3cd versus MMP-10cd binding selectivity for TIMP-1-C6 (with 8.3-fold improvement) and TIMP-1-C4 (with about 12-fold improvement) (Table 1). The K_i values measured using soluble TIMP-1 variant proteins are consistent with the yeast

surface display binding results and confirm that the expressed soluble TIMP-1 variants recapitulate the selectivity enhancements predicted by binding behavior on the yeast surface. Because WT TIMP-1 is a potent physiological inhibitor of MMP-9 (36), we also measured MMP-9cd inhibition of the MMP-3-selective TIMP-1 variants. Measuring the TIMP-1 variant K_i values with high accuracy was not possible using the tight inhibition-binding assay because of the considerably weakened inhibition of the selective variants toward MMP-9cd. Our data demonstrate that engineered MMP-3-selective TIMP-1 variants C4 and C6 only weakly inhibit MMP-9cd with considerably reduced K_i compared with WT TIMP-1, suggesting the potential for counter-selective screening with one MMP competitor to simultaneously decrease binding to other MMPs not included as competitors in the counterselection.

Crystal structures of TIMP-1-selective variants in complex with MMP-3cd and molecular models of complexes with MMP-10cd reveal alterations in TIMP–MMP interactions

To better understand the effect of TIMP-1 mutations on selective binding to MMP-3cd, we cocrystallized two of the most selective MMP-3cd binders isolated from counter-selective FACS, TIMP-1-C4 (L34G/M66D/T98G/P131S/Q153N), and TIMP-1-C6 (L34G/M66S/E67Y/L133N/S155L), in complex with MMP-3cd. We solved the TIMP-1-C4–MMP-

Engineering MMP-3-selective TIMP-1

A

Clone	AB	C-connector	EF	GH	MT
C4	L34G	M66D	T98G	P131S	Q153N
C5		M66G/E67N	T98D		
C6	L34G	M66S/E67Y		L133N	S155L
C9		M66G/E67H			
C10	L34G				S155L
C11	L34G	M66G/E67N			L151Q

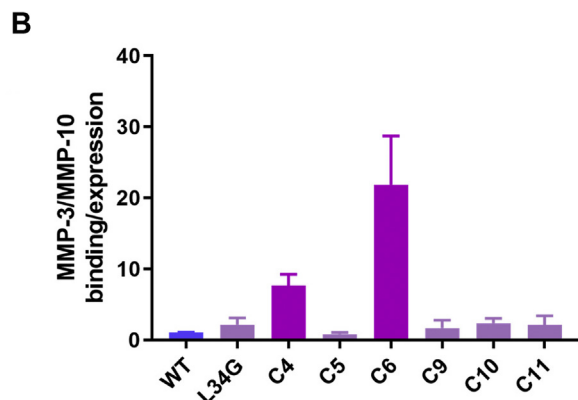


Figure 2. TIMP-1 variants isolated after counter-selective screening for MMP-3cd binding selectivity. A, TIMP-1 mutations found within the five MMP-interacting loops (AB, C-connector, EF, GH, and multiple-turn [MT] loops) for the most prevalent clones that were isolated and sequenced after five rounds of counter-selective screening for MMP-3cd versus MMP-10cd. B, the ratio of MMP-3cd binding to expression divided by MMP-10cd binding to expression for each clone tested on the yeast surface, normalized to WT TIMP-1 (WT, shown in blue). The clones with highest binding selectivity to MMP-3cd versus MMP-10cd (C4 and C6) are highlighted in magenta. MMP-3, matrix metalloproteinase 3; TIMP-1, tissue inhibitor of metalloproteinases 1.

3cd and TIMP-1-C6–MMP-3cd structures by molecular replacement and refined against diffraction data extending to resolutions of 3.00 and 2.34 Å, respectively. Data collection and refinement statistics are summarized in Table 2. The structures have been deposited in the Protein Data Bank (PDB) with accession numbers 7S7M and 7S7L, respectively. Each complex shows the expected protein architecture of TIMP-1 and MMP-3cd as described previously for MMP-3 complexes with WT TIMP-1 (PDB ID: 1UEA) (37) and other TIMP-1 variants engineered with improved binding affinity (PDB ID: 6MAV, 6N9D) (21). To enable structural comparisons capable of explaining the enhanced specificity of the variants for inhibition of MMP-3 in preference to MMP-10, we also modeled the complexes of these TIMP-1 variants with MMP-10cd using *in silico* mutagenesis and molecular dynamics simulations based upon our previously reported crystal structure of the complex of MMP-10cd with WT TIMP-1 (PDB ID: 3V96 (22)). Structural alignments and comparisons among the experimental and computational models highlighted multiple regions of variance at the intermolecular interface, as described later.

TIMP-1 mutation L34G in the AB-loop promotes formation of a tyrosine clasp uniquely with MMP-3

The single most common mutation among the selected and sequenced variants was L34G, a mutation found previously

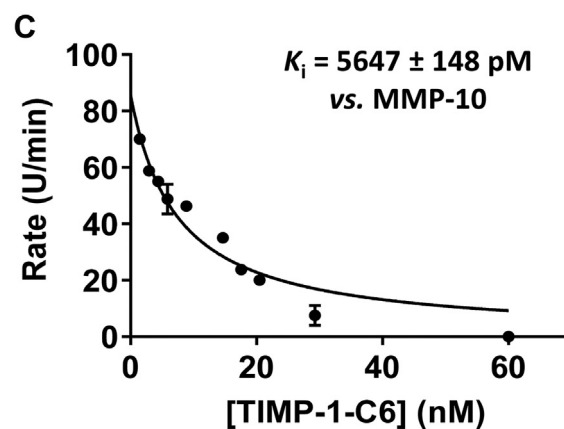
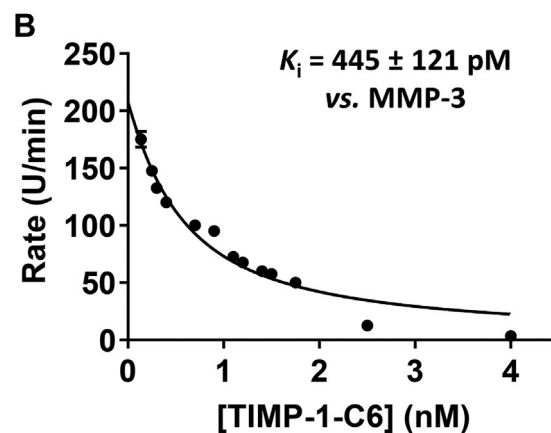
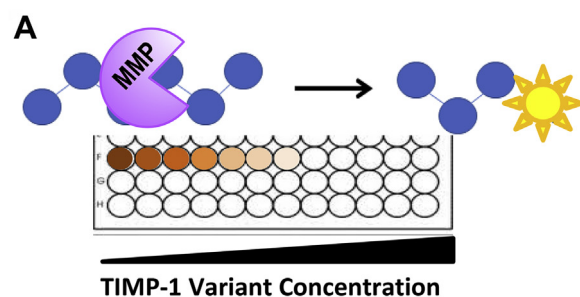


Figure 3. TIMP-1-C6 variant selectively inhibits MMP-3 in preference to MMP-10. A, schematic diagram shows inhibited cleavage of fluorogenic MMP substrate by increasing inhibitor concentrations in MMP activity assays. Initial velocities of substrate cleavage, measured over a 120 min time course, were plotted versus TIMP-1-C6 variant concentration for inhibition of MMP-3cd (B) and MMP-10cd (C). Data were fitted by multiple regression to Morrison's tight-binding inhibition equation to determine equilibrium inhibition constants (K_i). Data from representative experiments are shown; independent experiments were conducted in duplicate with K_i reported as average \pm SD. MMP-3, matrix metalloproteinase 3; TIMP-1, tissue inhibitor of metalloproteinases 1.

among TIMP-1 variants with enhanced MMP-3 affinity, and for which structural consequences have been previously described (21). In the new crystal structures of MMP-3cd complexes with TIMP-1-C4 and TIMP-1-C6 variants, we confirmed that this mutation in each case facilitates closer interaction between the MMP-3 S-loop and the TIMP-1 AB-loop (Fig. 4A). While hydrophobic contacts between TIMP-1 Leu34 and MMP-3 Phe154 are lost because of the mutation, this loss is more than compensated by formation of a

Table 1
Inhibition constants of soluble TIMP-1 variant proteins for inhibition of MMP-3cd, MMP-9cd, and MMP-10cd using tight-binding assays

TIMP-1 variant	K_i (pM)		
	MMP-3	MMP-9	MMP-10
WT TIMP-1	96.4 ± 8.9	1640 ± 260	153 ± 11
TIMP-1-C6	445 ± 121	>>10,000 ^a	5647 ± 148
TIMP-1-C4	255 ± 18	>>10,000 ^a	4827 ± 32

Reported values represent mean ± SD for duplicate independent experiments.

^a TIMP-1 C4 and C6 variants showed minimal inhibition of MMP-9cd such that K_i could not be determined in the tight-binding assay.

reciprocal tyrosine (Tyr) clasp in which TIMP-1 Tyr35 and MMP-3cd Tyr155 side chains each cross the intermolecular interface to form short H-bonds (range = 2.6–2.8 Å) with the partner protein backbone. The two Tyr residues simultaneously form favorable hydrophobic and edge-to-face π interactions with each other, bridging the interface (Fig. 4A). Consistent with the importance of this Tyr clasp for affinity, mutagenesis studies have shown that the TIMP-1 L34G single mutation confers approximately threefold enhanced affinity and inhibition toward MMP-3cd (21). The situation is different with MMP-10. Because of small differences in backbone positioning in the MMP-10cd–TIMP-1 complex, TIMP-1 Tyr-35 is not in close enough proximity to H-bond to the Phe154 carbonyl; it is 4.3 Å away in the crystal structure of MMP-10cd–WT TIMP-1 and is predicted to drift further away in MMP-10 complexes with TIMP-1-C4 and TIMP-1-C6 variants (Fig. 4B). As in the complex with MMP-3, the TIMP-1

L34G mutation results in loss of favorable hydrophobic interactions with Phe154 of MMP-10 as well, but in this case, without any compensating new intermolecular interactions involving the AB-loop. Thus, it appears that Tyr clasp formation enabled by the L34G mutation uniquely stabilizes the interaction of TIMP-1 variants with MMP-3 (but not MMP-10), contributing to selectivity in addition to affinity. The role of this mutation in selectivity is further supported by the observation of enhanced binding selectivity of the TIMP-1–L34G single mutant toward MMP-3cd *versus* MMP-10cd in the yeast display format (Fig. 2B).

TIMP-1 mutations in C-connector loop residues Met66 and Glu67 disrupt favorable interactions with MMP-10

Most of the selected and sequenced TIMP-1 variants possessed mutations in the C-connector loop at Met66, alone, or in combination with mutation of adjacent Glu67 (Fig. 2A). In the WT TIMP-1 complexes, Met66 does not form any interactions with MMP-3 but does form multiple hydrophobic contacts with MMP-10 that are not present in the MMP-3 complex. Whereas there is nonoptimal packing with no contact at the interface between Met66 and MMP-3 residues Ala169 and Asn175 (Fig. 5A), the analogous residues in MMP-10 are Pro185 and Tyr191, with which the TIMP-1 Met66 side chain forms hydrophobic contacts of 3.6 and 4.1 Å, respectively (Fig. 5B). The M66S mutation found in the TIMP-1-C6 variant is easily accommodated at the interface without significant impact on the complex with MMP-3, whereas the replacement with the smaller serine side chain disrupts the favorable packing of Met66 with Pro185 and Tyr191 in the complex with MMP-10 (Fig. 5, A and B). Replacement of Met66 with Asp in the TIMP-1-C4 variant similarly disrupts these favorable interactions with MMP-10, while having little impact on the looser interaction with MMP-3 in this region. In our crystal structure of TIMP-1-C4 bound to MMP-3, electron density for the Asp66 side chain was absent beyond the beta-carbon, reflective of an absence of interactions to stabilize this side chain in a single conformation. Modeling of potential conformations of Asp66 in both MMP-3 and MMP-10 complexes confirms the lack of potential interface interactions with this residue.

The impact of the E67Y mutation may be modestly deleterious for both MMP-3 and MMP-10 binding, with potentially greater disruption of interactions with MMP-10cd. In the complex of WT TIMP-1 with MMP-3, Glu67 forms a single H-bond with the backbone N of MMP-3 His211 (Fig. 5A). In the complex with MMP-10, Glu67 forms this same H-bond with the analogous His227 and also forms an intramolecular salt bridge with TIMP-1 Arg75 (Fig. 5B). Mutation of Glu67 to Tyr eliminates the H-bond in both MMP complexes. In the complex of TIMP-1-C6 with MMP-3, shape complementarity at the intermolecular interface is roughly maintained in this region because of stabilization of the conformation of Tyr67 by an intramolecular edge-to-face π interaction with the aromatic ring of Phe73 (Fig. 5A). The E67Y mutation may have a greater deleterious impact on MMP-10 binding since in this complex

Table 2
X-ray crystallographic data collection and refinement statistics

Structure name	TIMP-1-C4–MMP-3cd	TIMP-1-C6–MMP-3cd
PDB ID	7S7M	7S7L
Data collection		
Resolution range (Å)	15.63–3.00	47.60–2.34
Space group	P6522	P6522
<i>a</i> , <i>b</i> , <i>c</i> (Å)	69.28, 69.28, 318.98	69.33, 69.33, 312.22
α , β , γ (°)	90, 90, 120	90, 90, 120
R-merge	0.125 (0.772)	0.183 (0.951)
R-measure	0.152 (0.915)	0.190 (0.995)
R-pim	0.084 (0.485)	0.0477 (0.281)
CC1/2	0.943 (0.469)	0.987 (0.656)
Multiplicity	3.1 (3.4)	13.7 (10.7)
Completeness (%)	94.58 (99.64)	97.99 (93.77)
Mean <i>I</i> /sigma (<i>I</i>)	6.7 (1.2)	12.6 (1.9)
Refinement		
Unique reflections used in refinement	9264 (920)	19,481 (1811)
R-work/R-free	0.205/0.249	0.206/0.239
Number of nonhydrogen atoms	2559	2722
Macromolecules	2505	2614
Ligands	5	29
Solvent	49	79
Protein residues	333	340
RMSD bonds (Å)	0.008	0.005
RMSD angles (°)	1.29	1.02
Ramachandran favored (%)	95.4	96.4
Ramachandran outliers (%)	0.0	0.0
Average <i>B</i> -factor	79.9	55.6
Macromolecules	80.5	55.8
Ligands	66.3	53.0
Solvent	49.1	48.2

Values from highest resolution shell are shown in parentheses.

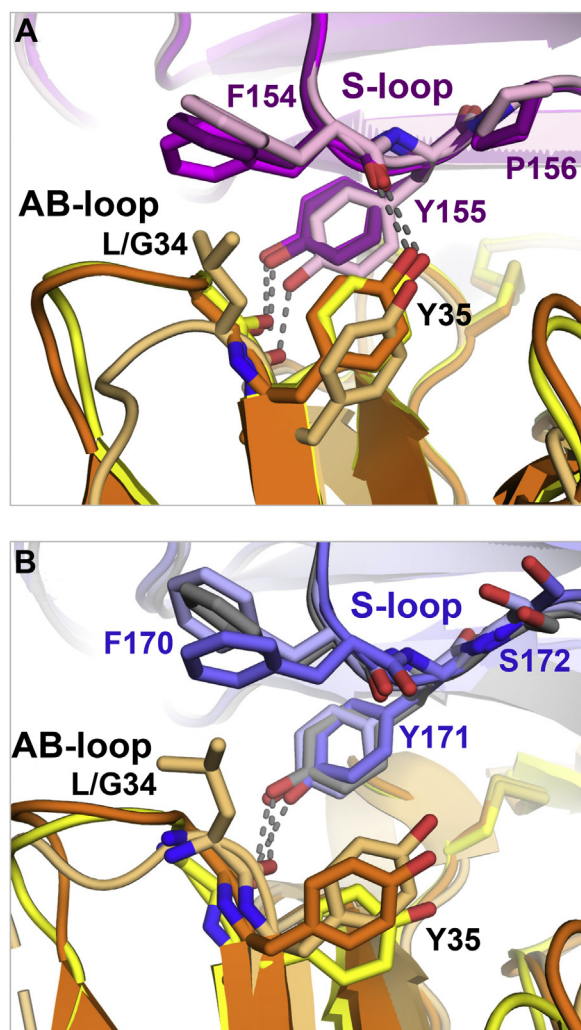


Figure 4. TIMP-1 L34G mutation strengthens interactions uniquely with MMP-3. *A*, crystal structures of TIMP-1-C4 (orange) bound to MMP-3cd (purple) and TIMP-1-C6 (yellow) bound to MMP-3cd (magenta) reveal formation of a reciprocal Tyr clasp characterized by two short interfacial H-bonds (gray dashed lines) combined with π interactions between the two involved Tyr, TIMP-1 Tyr35 and MMP-3 Tyr155. The looser interaction between WT TIMP-1 (peach) and MMP-3cd (pink) is shown for comparison, from PDB: 1UEA. Mutational ablation of the Leu34 side chain enables subtle backbone shifts that align the two Tyr residues to engage the clasp. *B*, molecular modeling of the complexes of TIMP-1-C4 (orange) and TIMP-1-C6 (yellow) bound to MMP-10cd (blue and periwinkle, respectively) compared with the WT TIMP-1 and MMP-10cd crystal structure (peach and gray, respectively; PDB: 3V96) predict no comparable new interactions with the TIMP-1 variants to compensate for loss of hydrophobic interactions between TIMP-1 Leu34 and MMP-10 Phe170. MMP-3, matrix metalloproteinase 3; PDB, Protein Data Bank; TIMP-1, tissue inhibitor of metalloproteinases 1.

the mutation results in elimination of both the intermolecular H-bond and the intramolecular salt bridge, which in this case is not predicted to be compensated by stabilizing aromatic interactions (Fig. 5B).

TIMP-1 mutations in the GH-loop and MTL-loop of the C-terminal domain disrupt favorable interactions with MMP-10 and create new interactions with MMP-3

Protein crystal structures and structural models of complexes with TIMP-1-C6 and TIMP-1-C4 also provide insight

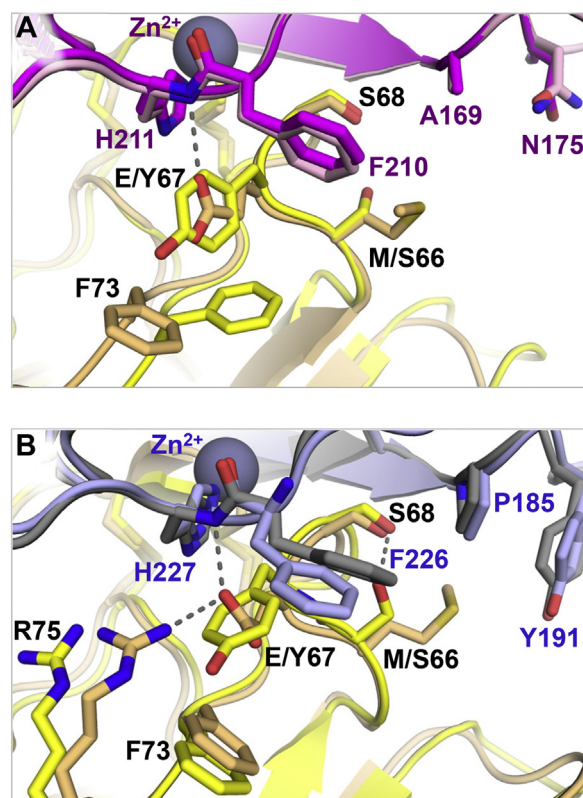


Figure 5. TIMP-1 C-connector loop mutations disrupt interactions more important for MMP-10 binding. *A*, crystal structure of TIMP-1-C6 (yellow) bound to MMP-3cd (magenta) compared with WT TIMP-1 (peach) and MMP-3cd (pink) from PDB: 1UEA show no interaction with the enzyme of either Met or serine (Ser) at position 66. Glu67 of WT TIMP-1 forms a single H-bond with the backbone amide of MMP-3 His211, whereas Tyr67 is stabilized in a sterically similar position via hydrophobic and ring-stacking interactions with TIMP-1-C6 Phe73. *B*, the WT-TIMP-1-MMP-10cd crystal structure (peach and gray, respectively; PDB: 3V96) shows close hydrophobic packing of TIMP-1 Met66 with MMP-10 residues Pro185 and Tyr191 and a network of H-bonds positioning TIMP-1 Glu67 between the backbone amide of MMP-10 His227 and side chain of TIMP-1 Arg75. All interface interactions with MMP-10cd (periwinkle) in this region are predicted to be disrupted by the M66S and E67Y mutations present in TIMP-1-C6 (yellow); the sole new interaction is an intramolecular H-bond between TIMP-1-C6 Ser66 and Ser68. MMP-10, matrix metalloproteinase 10; PDB, Protein Data Bank; TIMP-1, tissue inhibitor of metalloproteinases 1.

into how mutations in the TIMP-1 C-terminal domain modify selectivity of these selected variants. The TIMP-1-C6 variant contains the L133N mutation within the GH-loop, and the TIMP-1-C4 variant contains the nearby P131S mutation. Because of differences between MMP-3 and MMP-10 backbone conformations in this part of the interface, Leu133 shows different positioning and interactions in these complexes. In the complex of WT TIMP-3 with MMP-3, C_γ of Leu133 shows a single hydrophobic close contact (4.0 Å) with Tyr223 C_{e1}, and this packing is little changed by the L133N mutation (Fig. 6A). In TIMP-1-C4 containing the P131S mutation, subtle shifts in backbone conformation enhance intramolecular hydrophobic interactions between Leu133 and Val4, but interactions of Leu133 with MMP-3 Tyr223 are still limited to a single hydrophobic close contact (3.9 Å). In the complex of WT TIMP-1 with MMP-10, however, Leu133 is hugged in closer to both the MMP and the N-terminal domain

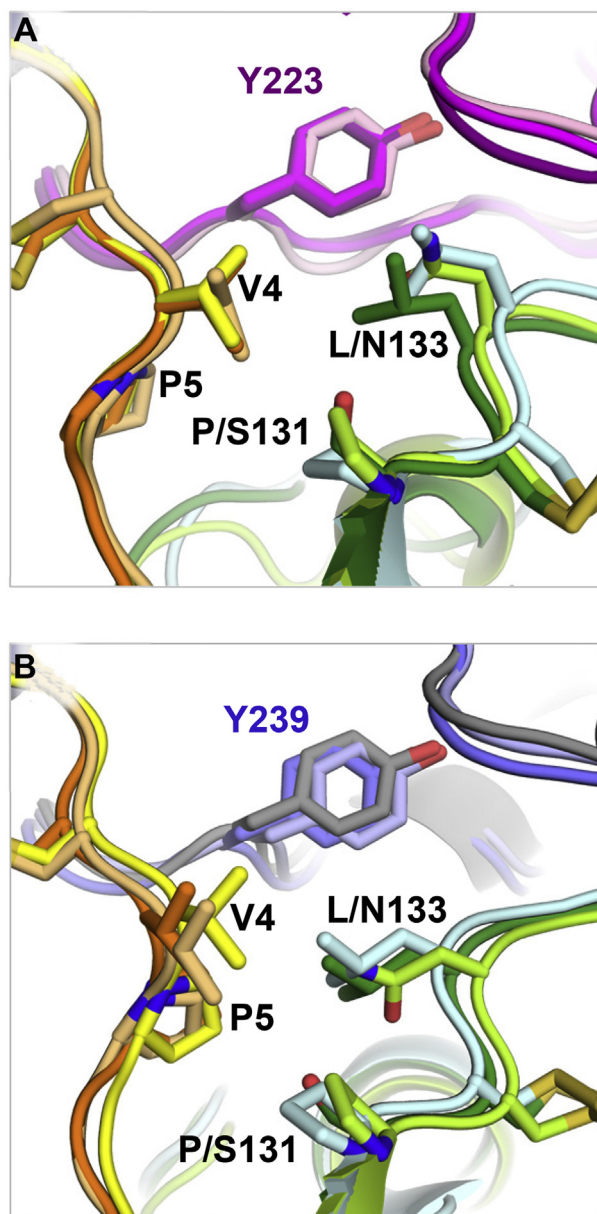


Figure 6. TIMP-1 L133N and P131S mutations weaken more extensive interactions with MMP-10. *A*, structure of WT TIMP-1 (N-terminal and C-terminal domains in *peach* and *aqua*, respectively) bound to MMP-3cd (*pink*) from PDB: 1UEA reveals a single close hydrophobic contact between TIMP-1 Leu133 C_γ and MMP-3cd Tyr223 C_{ε1} and little interaction between the two TIMP domains in this region. This packing is little changed by the L133N mutation in the crystal structure of TIMP-1-C6 (N-terminal and C-terminal domains in *yellow* and *lime*, respectively) bound to MMP-3cd (*magenta*). The crystal structure of TIMP-1-C4 containing the P131S mutation shows closer packing between Val4 of the N-terminal domain (*orange*) and Leu133 of the C-terminal domain (*forest*) but minimal interaction with Tyr223 of MMP-3 (*purple*). *B*, the WT-TIMP-1–MMP-10cd crystal structure (TIMP-1 colored as *aforementioned* and MMP-10cd in *gray*; PDB: 3V96) shows extensive close hydrophobic interactions between TIMP-1 C-terminal domain residue Leu66, MMP-10 Tyr239, and TIMP-1 N-terminal domain residues Val4 and Pro5. Pro131 forms close intramolecular contacts with Val4 and Leu133. Here, mutation L133N in TIMP-1-C6 (colored as *aforementioned*) is predicted to fully disrupt the extensive hydrophobic interactions between TIMP domains and with MMP-10 (*periwinkle*). Mutation P131S in TIMP-1-C4 (colored as *aforementioned*) disrupts intramolecular hydrophobic interactions between the TIMP-1 domains, loosening the interaction with MMP-10 Tyr239 (*blue*). MMP-10, matrix metalloproteinase 10; PDB, Protein Data Bank; TIMP-1, tissue inhibitor of metalloproteinases 1.

of the TIMP, forming multiple hydrophobic contacts with MMP-10 Tyr239 (4.0 and 4.1 Å) and with TIMP-1 Val4 (3.8 and 4.0 Å) and Pro5 (4.1 Å) (Fig. 6B). These favorable packing interactions are all predicted to be lost in the TIMP-1-C6 variant with its L133N mutation (Fig. 6B). In the WT-TIMP-1–MMP-10 complex, the complementarity of the inhibitor to the MMP in this region is further stabilized by close intramolecular hydrophobic packing of Pro131 with both Leu133 and Val4; these stabilizing contacts are lost in TIMP-1-C4 because of the P131S mutation, and consequently the interaction of Leu133 with MMP-10 Tyr223 weakens, with predicted closest distance of 4.4 Å. Thus, the L133N and P131S mutations are both anticipated to be neutral for MMP-3 binding but deleterious for MMP-10 binding.

In the multiple turn loop of TIMP-1, mutations were observed at Q153N in TIMP-1-C4 and S155L in TIMP-1-C6. Our structures of the TIMP-1 variant complexes with MMP-3cd reveal altered backbone conformations in the MTL-loop as a result of these amino acid substitutions (Fig. 7A). In the case of the TIMP-1-C4 variant, it is not clear whether the Q153N substitution directly impacts binding or specificity, as neither residue at this position appears to make direct contact with either MMP. However, the S155L mutation found in the TIMP-1-C6 variant may potentially enhance selectivity for MMP-3 over MMP-10. The WT TIMP-1 complex with MMP-3cd features a single intermolecular contact in this region, an H-bond between the TIMP-1 Glu156 and MMP-3 Tyr220 side chains. The shift of the TIMP-1 backbone in the TIMP-1-C6 variant results in replacement of this interaction with new hydrophobic packing interactions of the newly introduced Leu155 side chain with MMP-3 Leu222 (3.6 and 4.0 Å) and TIMP N-terminal domain residue Pro5 (4.1 Å). In the MMP-10 complexes, by contrast, the variant substitutions in the MTL-loop are not predicted to substantially alter direct interactions with the enzyme, where the H-bond between TIMP-1 Glu156 and MMP-10 Tyr236 is the only close contact observed in all complexes (Fig. 7B). Thus, the S155L mutation of TIMP-1-C6 may modestly shift specificity in favor of MMP-3 inhibition through enhanced hydrophobic packing.

Discussion

Protein engineering using yeast surface display is a powerful tool for improving binding affinity and selectivity of protein binders and has been widely used to engineer scaffolds such as antibodies (38, 39). Protein engineering *via* directed evolution can also be used to unravel protein sequence–structure–function relationships and understand the detailed mechanisms of natural and engineered protein–protein binding interactions (40). Here, we used a combination of rational protein design, directed evolution, and structural analyses to evolve variants of TIMP-1 capable of fine discrimination between closely related MMPs and to dissect the sequence and structural features responsible for the evolved specificity. We used a counter-selective screening strategy to isolate TIMP-1 variants with markedly improved binding selectivity for

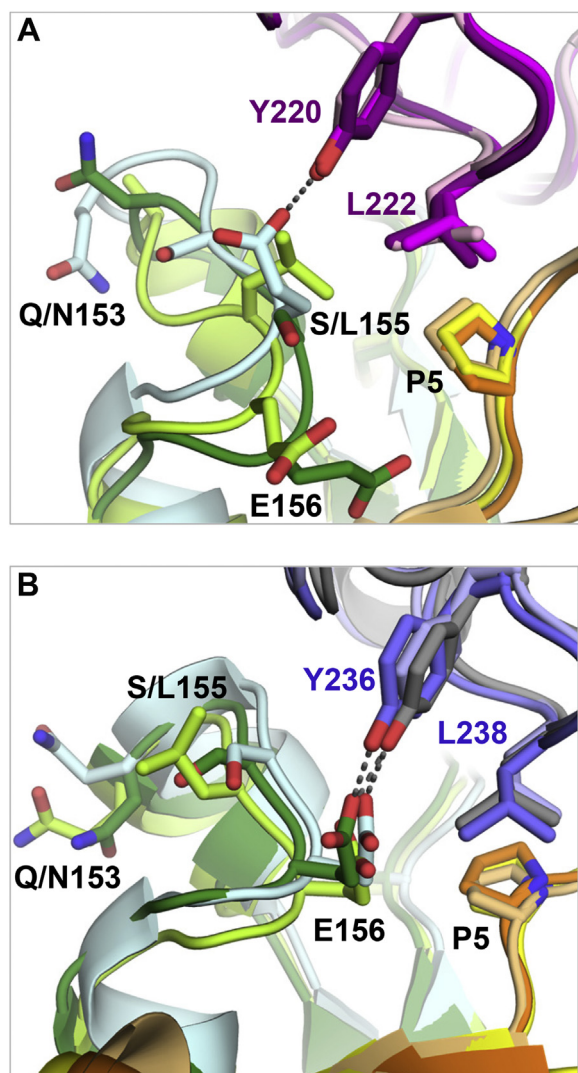


Figure 7. Mutations in the TIMP-1 multiple turn loop introduce new intermolecular and intramolecular interactions in MMP-3 complexes. *A*, structure of WT TIMP-1 (N-terminal and C-terminal domains in *peach* and *aqua*, respectively) bound to MMP-3cd (*pink*) from PDB: 1UEA reveals a single H-bond between TIMP-1 Glu156 and MMP-3cd Tyr220 side chains and little interaction between the two TIMP domains in this region. Substantial conformational changes are seen in the multiple turn loops of TIMP-1-C4 (N-terminal and C-terminal domains in *orange* and *forest*, respectively) bound to MMP-3cd (*purple*) and TIMP-1-C6 (N-terminal and C-terminal domains in *yellow* and *lime*, respectively) bound to MMP-3cd (*magenta*). In the MMP-3cd-TIMP-1-C6 complex, this results in new hydrophobic interactions of TIMP-1-C6 Leu155 with MMP-3cd Leu222 and TIMP-1-C6 N-terminal domain residue Pro5. *B*, the crystal structure of WT TIMP-1 (colored as aforementioned) with MMP-10cd (*gray*) (coordinates from PDB: 3V96) and models of TIMP-1-C4 and TIMP-1-C6 (colored as aforementioned) in complex with MMP-10cd (*blue* and *periwinkle*, respectively) show little difference among the WT and mutant complexes. MMP-3, matrix metalloproteinase 3; PDB, Protein Data Bank; TIMP-1, tissue inhibitor of metalloproteinases 1.

MMP-3 compared with MMP-10, the most closely related MMP in terms of sequence homology, protein structure, and substrate specificity. Thus, our study provides proof of principle for the capability of full-length TIMPs to serve as scaffolds for development of highly selective MMP inhibitors and demonstrates the utility of our yeast surface display platform and counter-selective screening strategy to achieve desired specificity.

MMPs play multifaceted roles in many diseases, and while overexpression or elevated activity of specific MMPs possess demonstrated roles in driving disease pathogenesis, there are many examples in which other MMPs can have opposing beneficial effects in the same disease setting (9, 10, 41). This effect likely underlies the poor performance of broad-spectrum MMP inhibitors in clinical trials for cancer and arthritis, since they targeted beneficial MMPs alongside those representing drivers of pathology, and showed poor tolerability because of off-target side effects (1, 6–8, 42). Consequently, much more selective inhibitors are desired, but selective small-molecule inhibitors have been notoriously difficult to develop for the MMPs because of very close structural homology in the vicinity of the active site among the many members of this enzyme family. Compared with small-molecule ligands, protein-based inhibitors can offer greater opportunities to generate specificity because they interact with target proteins utilizing much broader contact surfaces. Here, we have taken advantage of the natural protein scaffold of full-length TIMP-1, which has evolved to uniquely target active metalloproteinase catalytic domains utilizing a contact interface of $>1200 \text{ \AA}^2$. Notably, the targeted contact interface on the MMP extends beyond the conserved active site to include less-conserved exosites on the catalytic domain, conferring considerable potential to engineer specificity (23).

Several other recent strategies have aimed to engineer selective protein-based MMP inhibitors by employing diversity library screening of single-chain antibodies or single domain TIMP constructs. Libraries of single-chain antibodies generated by immunization of llamas with an active human MMP-10-Fc fusion protein were displayed on yeast and enriched for MMP-10 binders. Among the MMP-10 binders identified in this screen were four that inhibited MMP-10 activity, one of which turned out to be selective for MMP-10 over MMP-3 (43). Phage and yeast displayed libraries of engineered antibody domains have also been screened to identify various selective inhibitors of MMP-14, as we have reviewed previously (1). In one example, an MMP-selective human Fab, engineered with an extended convex antigen-binding site resembling that of camelid antibodies, was isolated using a phage display approach and shown to inhibit MMP-10 in preference to MMP-2 or MMP-9 (44). Some of the challenges of developing such MMP-targeted antibodies are that many antibodies raised against the MMP immunogen will not bind in an inhibitory fashion, and others will not distinguish between active MMP and inactive zymogen. Thus, it may be only a very small proportion of the library that possess these desired characteristics.

By contrast, when using a TIMP-based library to engineer selective MMP inhibitors, the entire library is based on a scaffold that is uniquely evolved to bind to the active site of active MMPs in a completely inhibitory fashion. Here, the greater challenge becomes evolving selectivity among MMPs, since native TIMPs broadly inhibit most MMPs. Earlier studies employed the isolated N-terminal domain of TIMP-2 as a scaffold for engineering selective inhibitors of MMP-14 and

MMP-9 (17, 18). In addition to the core inhibitory epitope that binds in the enzyme active site, this domain includes the TIMP AB-loop, which contacts the MMP catalytic domain at a nonconserved surface exosite, giving opportunities for evolution of specificity. In the present study, by employing full-length TIMP-1 as a scaffold, we added epitopes of the TIMP C-terminal domain, specifically the multiple-turn loop and the GH-loop, that confer additional opportunities for selectivity by embracing additional exosites on the MMP catalytic domain. Furthermore, we also employed a competitive screening strategy, which provided not only positive selection for our target (MMP-3cd) but also negative selection for undesired binders, here the most similar member of the MMP family (MMP-10cd). Our sequencing and structural analyses reveal that mutations in multiple loops of both N-terminal and C-terminal domains contribute to improvements in specificity. Furthermore, since these mutations appear in regions of structural plasticity and result in substantial alterations to proximal TIMP-1 backbone conformations, which are differently configured in the complexes with each MMP, our results are unlikely to have been achieved by previous methods of screening. In other words, our counter-selective screening approach directed the evolution of TIMP-1 binding selectivity in an unconventional path, which could not have been easily predicted by computational studies, nor were the selective variants identified through FACS screening toward MMP-3 alone in our earlier study (21). Importantly, the competitive screening approach employed here succeeded at identifying selective inhibitors capable of discrimination between the two most closely related MMPs, suggesting that it should also be capable of similarly identifying inhibitors selective for any other MMP.

MMP-3 has been regarded as a potential therapeutic target for several different inflammatory and degenerative diseases. For example, we have shown that MMP-3 is upregulated in patients with IPF, where it mediates pathogenic processes *via* cleavage of E-cadherin to activate epithelial to mesenchymal transition (31, 32). MMP-3-null mice are protected against bleomycin-induced pulmonary fibrosis, suggesting that selective MMP-3 inhibition might offer an effective therapeutic strategy to treat IPF. MMP-3 is likewise upregulated in inflammatory responses of acute lung injury (ALI) and ARDS, where it is a pivotal mediator of, and therapeutic target in, the pathological processes that underlie these diseases (33–35, 45–47). Mice genetically deficient in MMP-3 have been found to be protected from ALI in several preclinical models (33, 34), suggesting the therapeutic potential of selective MMP-3 inhibition for treatment of ALI–ARDS.

Several other MMPs are also upregulated in lung diseases or are constitutively present in the lung, including some that appear to have protective or mixed effects on disease progression, and thus may represent antitargets in the development of MMP-3 inhibitory strategies. In the inflammatory setting triggered by acute infection, MMP-10 produced by macrophages moderates inflammation and protects against tissue damage (41, 48, 49). Similar protective effects are seen in

lung injury caused by inhalation of long multiwalled carbon nanotubes (50). Studies of MMP-9 in lung disease have shown context-dependent profibrotic and antifibrotic effects in different models of lung fibrosis (51). In models of lung injury induced by mechanical ventilation or by ozone inhalation, MMP-9 was shown to have protective functions, and MMP-9-null mice developed more severe injury than WT mice in these models (52, 53). Other MMPs that demonstrated protective roles in lung disease include MMP-19, which protects against the development of lung fibrosis (54), MMP-13, which moderates inflammation in ALI (55) and promotes resolution of lung fibrosis (56, 57), and MMP-28, which regulates macrophage polarization and infiltration into sites of acute lung infection (41, 58). In this study, we engineered TIMP-1 variants that retained strong inhibitory capability toward MMP-3 while significantly reducing inhibition of MMP-10 and eliminating observed inhibition of MMP-9, thus taking strides toward the selectivity profile desired for an MMP-targeting therapeutic for lung diseases.

In conclusion, we have demonstrated that the full-length TIMP-1 protein can be engineered for fine discrimination between the most similar of MMPs. We developed a promising protein engineering selection strategy that holds great promise for further fine-tuning of MMP-3-selective inhibitors as well as selective inhibitors of other MMPs of clinical interest as therapeutic targets. Our structural studies defined the subtle alterations in TIMP–MMP interactions resulting from the selected mutations that are responsible for shifts in selectivity. Together, our results showcase the considerable power of structure-based library design combined with directed evolution using yeast surface display and counter-selective FACS screening. This protein engineering approach can be extended to protein therapeutic development based on other natural enzyme inhibitors, critically improving selectivity to eliminate off-target effects.

Experimental procedures

Strains and plasmids

Yeast DNA vectors for displaying TIMP-1 variants at the N terminus of Aga2p protein on the yeast surface were derived from the pCHA backbone, pCHA-VRC01 vector (59), as described previously (21). For the yeast display of full-length human TIMP-1 and TIMP-1 variants, the yeast *Saccharomyces cerevisiae* strain EBY100 (MATa AGA1::GAL1-AGA1::URA3 *ura3-52 trp1 leu2-delta200 his3-delta200 pep4::HIS3 prb11.6R can1 GAL*) was purchased from American Type Culture Collection.

MMP expression, purification, and biotinylation

MMP catalytic domain proteins lacking the C-terminal hemopexin domain were expressed in zymogen form (pro-MMP) using a pET-3a vector. pET3-MMP-3cd was a generous gift of Nagase *et al.* (60). ProMMP-3cd was refolded and purified after bacterial expression and extraction from inclusion bodies as described previously (21, 60). The denatured protein

Engineering MMP-3-selective TIMP-1

was purified on Q-Sepharose and then refolded by stepwise dialysis, followed by activation overnight in the presence of the organomercurial compound 4-aminophenyl mercuric acetate (61–63) according to our published protocols (21). ProMMP-10cd was expressed, purified, and activated using protocols similar to those for proMMP-3cd, as we have previously described (22). To minimize degradation, MMP-10 was activated for 1 h, and then the active MMP-10cd was quickly purified from residual proMMP-10cd and degradation products by gel filtration on Superdex 75 (22). An expression construct for production of truncated human pro-MMP-9 (residues 20–444; proMMP-9cd) was generated by PCR amplification of the gene from a human complementary DNA construct corresponding to GenBank accession ID BC006093 (Open Biosystems) using PCR primers 5'-CCATTTCA-TATGGCCCCCAGACAG-3' and 5'-CCCAGCA-GATCTTCATCAACCATAGAGGTG-3'. The PCR product was digested with NdeI and BglII (New England Biolabs) and cloned into vector pET-3a digested with NdeI and BamHI (New England Biolabs). The protein was expressed from *Escherichia coli* strain BL21(DE3), purified from inclusion bodies by Q-sepharose chromatography, and refolded essentially as described previously (64). MMP-9cd was activated by MMP-3cd using a proMMP-9cd:MMP-3cd molar ratio of 150:1 in 20 mM Tris, pH 7.5, and 10 mM CaCl₂, incubated for 30 min at 37 °C. MMP-3cd and MMP-10cd were biotinylated using the EZ-Link NHS-PEG4 biotinylation kit (Thermo Fisher Scientific) according to the manual with addition of biotin in 1:10 molar ratio (protein to biotin) and incubated at room temperature for 30 min. The biotinylated MMPs were purified using Zeba spin desalting columns (Thermo Fisher Scientific) and tested for degree of biotinylation using the 4'-hydroxyazobenzene-2-carboxylic acid assay according to the kit protocol.

Soluble TIMP-1 expression and purification

For expression of full-length human TIMP-1 and TIMP-1 variant proteins, the mammalian protein expression vector pTT-TIMP-1 was used (65). The TIMP-1 mutant genes were amplified from the corresponding yeast pCHA plasmids using PCR and inserted into the pTT-TIMP-1 vector using HindIII and BamHI restriction enzymes. WT TIMP-1 and TIMP-1 variants were expressed in human embryonic kidney 293-FreeStyle cells (Thermo Fisher Scientific) and purified by ion exchange and size-exclusion chromatography as previously described (21). TIMP-1 protein concentration was measured using titration against MMP-3cd protein stock of known concentration as previously described (21). TIMP-1 variant proteins were deglycosylated with peptide:N-glycosidase F (New England Biolabs) according to the manufacturer's protocols to prepare homogenous proteins for crystallization. Deglycosylated TIMP-1 C4 and C6 variant proteins were purified by size-exclusion chromatography using a Superdex-75 column (GE Healthcare) using 50 mM Hepes, pH 6.8, containing 150 mM NaCl equilibration and

elution buffer. The highly pure deglycosylated TIMP-1 fractions were combined and concentrated using Amicon Ultra-15 centrifugal filter units with molecular weight cutoff of 10 kDa.

Counter-selective screening of TIMP-1 targeted mutant library

Generation of the yeast display library of five million TIMP-1 variants with random mutations located within five MMP-interacting loops as shown in Figure 1A (3–4 mutations on an average per variant) and our general yeast culture, staining, and sorting methodology have been previously described in detail (21). Prior to each round of sorting, yeast cells were grown and induced, counted (absorbance of 1 at 600 nm = 10⁷ cells/ml), and then incubated with a mixture of biotinylated-MMP3cd and unlabeled MMP-10cd in phosphate-buffered saline with albumin (PBSA) buffer (8 g/l NaCl, 0.2 g/loading l KCl, 1.44 g/l Na₂HPO₄, 0.24 g/l KH₂PO₄ [pH 7.4], and 1% bovine serum albumin) for 1 h on ice. Cells were then washed and resuspended in cold PBSA buffer containing anti c-myc 9e10 (Sigma) and streptavidin Alexa Fluor 647 (each 1:100 dilution) on ice for 30 min and then washed with cold PBSA buffer and incubated with fluorescein-conjugated goat antimouse secondary antibody (Thermo Fisher Scientific) on ice covered from light for 30 min, before final washing and suspension in cold PBSA. Samples were maintained on ice until run on a cell sorter for library sorting (BD Aria II). Sorted cells were recovered in synthetic defined medium with casamino acid (pH 4.5) (20 g/l dextrose, 6.7 g/l yeast nitrogen base, 5 g/l Bacto casamino acids, 10.4 g/l sodium citrate, and 7.4 g/l citric acid monohydrate) containing 1% penicillin-streptomycin and incubated at 30 °C overnight. Yeast surface protein expression was induced by culturing cells in synthetic galactose casamino acid media (20 g/l galactose, 6.7 g/l yeast nitrogen base, 5 g/l Bacto casamino acids, 10.4 g/l sodium citrate, and 7.4 g/l citric acid monohydrate) at 30 °C overnight. The initial library (approximately 5 × 10⁷ yeast) was subjected to one round of screening (staining, sorting, recovery, and regrowth) using a concentration of 25 nM biotinylated MMP-3cd in the absence of MMP-10cd. Screening was continued through four additional rounds, for a total of five rounds, under equilibrium sorting conditions employing incrementally increasing unlabeled MMP-10cd concentration from 100 to 1000 nM.

DNA sequencing

Following rounds of sorting, recovered yeast was cultured on synthetic defined medium with casamino acid plates, and plasmid DNA was extracted from the isolated individual yeast clones using the Zymoprep Yeast Plasmid Miniprep II Kit (ZymoResearch). TIMP1 mutant genes were amplified using PCR with primers upstream and downstream of the TIMP1 gene, and gel-purified PCR product was submitted for sequencing (Eurofins Scientific). Alternatively, plasmids extracted from yeast were transformed into *E. coli*, extracted and purified from bacteria using the QIAGEN Miniprep kit

(QIAGEN), and submitted for sequencing. Sequences were analyzed using SnapGene software (SnapGene, GSL Biotech, LLC).

Yeast surface display and flow cytometry of individual TIMP-1 variants

Individual selected pCHA-TIMP-1 variant plasmids were transformed into yeast strain EBY100 by electroporation, then grown, induced, harvested, stained, and analyzed by flow cytometry using protocols similar to those described previously (21). The yeast cells displaying TIMP-1 variants were first incubated with 100 to 250 nM biotinylated MMP-3cd or MMP-10cd in PBSA buffer for 1 h on ice, followed by anti c-myc and streptavidin Alexa Fluor 647 (each 1:100 dilution in PBSA buffer) for 30 min, and finally fluorescein-conjugated secondary antibody for 30 min. After harvesting and washing with cold PBSA, cells were centrifuged and resuspended in 750 μ l of PBSA buffer and then run through an Attune Nxt flow cytometer (Thermo Fisher Scientific). Flow cytometry data were collected from at least from 10,000 cell events per sample and analyzed using FlowJo software (FlowJo, LLC).

TIMP-1–MMP inhibition studies

K_i s of WT TIMP-1 and TIMP-1 variants toward MMP-3cd, MMP-10cd, and MMP-9cd were measured using a method appropriate for tight-binding inhibition, as we have described previously (17, 21). MMP-3cd (0.24 nM) or MMP-10cd (0.3 nM) was incubated with 0.04 to 2.5 nM WT TIMP1 or TIMP1 variant in TCNB buffer (50 mM Tris, pH 7.5, 100 mM NaCl, 10 mM CaCl₂, and 0.05% Brij) for 1 h at 37 °C. For MMP-9cd (0.3 nM), the range was 0.05 to 20 nM WT TIMP1 or TIMP1 variant using the same buffer and incubation time. Thereafter, the fluorogenic substrate Mca-Pro-Leu-Gly-Leu-Dpa-Ala-Arg-NH₂ [where Mca is (7-methoxycoumarin-4-yl) acetyl, Dpa is *N*-3-(2,4-dinitrophenyl)-L-2,3-diaminopropionyl] (AnaSpec) was added to the reaction at a final concentration of 10 μ M, and fluorescence was monitored with 340/30 excitation and 400/30 emission filters using a Synergy 2 plate reader (BioTek) at 37 °C. Fluorescence readings were recorded every minute for 120 min, and enzymatic rates were determined from the slope of the linear portion of the fluorescence signal. To determine K_i , data were plotted as initial velocities *versus* TIMP concentration and fitted by multiple regression to Morrison's tight-binding inhibition equation (66) (Equation 1), where V_t = enzyme velocity in the presence of inhibitor; V_0 = enzyme velocity in the absence of inhibitor; $[E]$ = enzyme concentration; $[I]$ = inhibitor concentration; $[S]$ = substrate concentration, K_m is the Michaelis–Menten constant, and K_i^{app} is an apparent inhibition constant given by Equation 2. Data were fitted using Prism 7 (GraphPad Software, Inc). Reported inhibition constants are average values obtained from two independent experiments, each with duplicate samples, and reported errors reflect standard deviation between the independent experiments. Calculations were performed using a K_m value of 11.23 μ M for MMP-3cd, 13.8 μ M for MMP-10cd,

and 2 μ M for MMP-9cd as determined from Michaelis–Menten kinetic experiments performed in triplicate in our laboratory.

$$\frac{V_t}{V_0} = \frac{1 - ([E] + [I] + K_i^{\text{app}}) - \sqrt{([E] + [I] + K_i^{\text{app}})^2 - 4[E][I]}}{2[E]} \quad (1)$$

$$K_i^{\text{app}} = K_i \left(1 + \frac{[S]}{K_m} \right) \quad (2)$$

Crystallization, X-ray diffraction, structure determination, and refinement

TIMP-1 variants and MMP-3cd protein were mixed at a molar ratio of 1:1 and then TIMP-1–MMP-3cd protein complexes were concentrated to \sim 3 to 5 mg/ml prior to crystallization screening. Crystals were grown *via* the hanging drop method, by mixing the protein solution 1:1 (v/v) with a reservoir solution (67). TIMP-1-C4–MMP-3cd protein crystals grew in condition 92 of the Top96 crystallization kit (Anatrace) (0.1 M ammonium acetate, 0.1 M Bis–Tris:HCl, pH 5.5, 17% [w/v] PEG 10000). TIMP-1-C6–MMP-3cd protein crystals grew in condition 65 of the Top96 crystallization kit (0.2 M ammonium sulfate, 0.1 M Bis–Tris:HCl, pH 6.5, 25% [w/v] PEG 3350). TIMP-1 variant–MMP-3cd protein crystals appeared in a few days and were grown over a few weeks. Crystals were flash cooled in liquid nitrogen using cryoprotectant buffer containing 30% dextrose. Single wavelength (1 Å) native X-ray diffraction data were collected at 100 K at Advanced Light Source beamline 8.2.1, Lawrence Berkeley National Laboratory. TIMP-1 variant complex structures were each solved from single crystals that diffracted to 3.00 Å (for TIMP-1-C4–MMP-3cd) and 2.37 Å resolutions (for TIMP-1-C6). The X-ray data were processed with iMOSFLM (68) for indexing, refinement, and integration with POINTLESS (69) and AIMLESS (70) for scaling and merging. The TIMP-1-C4–MMP-3cd dataset had faint ice rings, and efforts were made to reduce their impact without discarding useful data, utilizing the French and Wilson data correction tool within the Phenix suite. These efforts yielded fully interpretable electron density maps and reasonable data collection statistics. Free-R flags were assigned to a random 5% of reflections, and this test set was maintained throughout all subsequent stages of structure solution and refinement. X-ray crystal structures of the protein complexes of MMP-3cd–TIMP-1 variants were solved by molecular replacement using the program Molrep (71) (MMP-3cd–TIMP-1-C4) or Phaser (72, 73) (MMP-3cd–TIMP-1-C6). The previously solved structure of human MMP3cd–WT TIMP-1 (PDB ID: 1UEA) without the corresponding Zn and Ca ions was used as a search model. Following molecular replacement, Phenix.refine was used for sequential refinements (74) alternating with manual alterations in COOT software (75). After several stages of refinement, translation/libration/screw (TLS) parameters were determined *via* a tool within phenix.refine, which is a rapid implementation of the

Engineering MMP-3-selective TIMP-1

TLS motion determination method (76). For C4, a total of 15 TLS groups were determined, eight in MMP-3 and seven for TIMP-1; for C6, a total of 15 TLS groups were determined, seven for MMP-3 and eight for TIMP-1. As refinement progressed, spherical electron density peaks within hydrogen bonding distance to polar moieties became visible, and water was placed into them. Some highly flexible regions were not visible in electron density and left unmodeled. These residues included N-terminal residues 83 to 87 and C-terminal residues 248 to 255 of MMP-3cd and flexible loop residues 52 to 57 and C-terminal residues 180 to 184 of TIMP-1-C4 in PDB (ID: 7S7M); and C-terminal residues 248 to 255 of MMP-3cd and flexible loop 53 to 57 and C-terminal residues 181 to 184 of TIMP-1-C6 in PDB (ID: 7S7L). Structure figures were generated using PyMOL (Schrodinger, LLC).

Molecular modeling

Models of MMP-10-bound mutant TIMP-1 complexes were created starting from atomic coordinates for MMP-10–TIMP-1 (PDB: 3V96) (22) using methods that we have described in detail previously (77–79). Heteroatoms except coordinated metal ions were removed, as were alternative conformations of residues. Missing side chains were built with maximum likelihood rotamer assignment, and missing residues of TIMP-1 (25–30 and 50–57) were built using the TIMP-1 chain from the MMP-3–TIMP-1 crystal structure (PDB: 1UEA) (37) as a template. Mutations present in TIMP-1-C4 or TIMP-1-C6 were inserted with PyMOL's mutation wizard, picking the most optimal rotamer. These models were imported into YASARA (80), where hydrogens were added and metal ions parameterized with zero order bonds. A cubic simulation box was generated with axes 15 Å from protein atoms. Within the simulation box, transferable intermolecular potential 3P water models were inserted at a density of 0.997 g/l and Na⁺/Cl[−] counterions were randomly distributed at 0.9% (150 mM) final ionic strength. The pH was set to 7.4, pressure to 1 bar, and protonation states were adjusted based on pK_a. Solvent-simulated annealing was performed to slowly ramp the temperature from cryogenic 80 K to physiological 310 K, after which the entire system was subjected to steepest descent energy minimization for 2000 fs.

Data availability

The crystal structures of MMP-3cd–TIMP-1 variant complexes have been deposited in the PDB, www.rcsb.org (PDB IDs: 7S7L and 7S7M).

Supporting information—This article contains supporting information.

Acknowledgments—We thank Dr Laura Lewis-Tuffin in the Mayo Clinic cell sorting facility for assistance with FACS of TIMP-1 libraries. The ALS-ENABLE beamlines are supported in part by US National Institutes of Health grant P30 GM124169-01. The Advanced Light Source is a Department of Energy Office of Science User Facility under contract no. DE-AC02-05CH11231.

Author contributions—M. R.-S. and E. S. R. conceptualization; M. R.-S. and E. S. R. methodology; M. R.-S., M. C., and E. S. R. validation; M. R.-S., M. C., B. S., and E. S. R. formal analysis; M. R.-S., M. C., S. M., A. H., and B. S. investigation; A. H., B. S., and E. S. R. resources; M. R.-S., M. C., and E. S. R. data curation; M. R.-S., M. C., and E. S. R. writing—original draft; M. R.-S., M. C., B. S., G. P. D., D. C. R., and E. S. R. writing—review & editing; M. R.-S. and E. S. R. visualization; M. R.-S., G. P. D., D. C. R., and E. S. R. supervision; M. R.-S. and E. S. R. project administration; G. P. D., D. C. R., and E. S. R. funding acquisition.

Funding and additional information—This work was supported by US National Institutes of Health grants (R01 GM132100 and R01 CA258274 [to E. S. R.], R01 HL157424 [to G. P. D., D. C. R., and E. S. R.]) and US Department of Defense grant (grant no.: W81XWH-16-2-0030 [to G. P. D. and D. C. R.]). M. R.-S. is supported in part by National Institutes of Health grant (grant no.: P20 GM103650). The content is solely the responsibility of the authors and does not necessarily represent the official views of the National Institutes of Health.

Conflict of interest—The authors declare that they have no conflicts of interest with the contents of this article.

Abbreviations—The abbreviations used are: ALI, acute lung injury; ARDS, acute respiratory distress syndrome; FACS, fluorescent-activated cell sorting; IPF, idiopathic pulmonary fibrosis; MMP, matrix metalloproteinase; PBSA, phosphate-buffered saline with albumin; PDB, Protein Data Bank; TIMP, tissue inhibitor of metalloproteinases.

References

1. Radisky, E. S., Raeeszadeh-Sarmazdeh, M., and Radisky, D. C. (2017) Therapeutic potential of matrix metalloproteinase inhibition in breast cancer. *J. Cell. Biochem.* **118**, 3531–3548
2. Radisky, E. S., and Radisky, D. C. (2015) Matrix metalloproteinases as breast cancer drivers and therapeutic targets. *Front. Biosci. (Landmark Ed.)* **20**, 1144–1163
3. Hu, J., Van den Steen, P. E., Sang, Q. X., and Opdenakker, G. (2007) Matrix metalloproteinase inhibitors as therapy for inflammatory and vascular diseases. *Nat. Rev. Drug Discov.* **6**, 480–498
4. Murphy, G., and Nagase, H. (2008) Progress in matrix metalloproteinase research. *Mol. Aspects Med.* **29**, 290–308
5. Kessenbrock, K., Plaks, V., and Werb, Z. (2010) Matrix metalloproteinases: Regulators of the tumor microenvironment. *Cell* **141**, 52–67
6. Fingleton, B. (2008) MMPs as therapeutic targets—still a viable option? *Semin. Cell Dev. Biol.* **19**, 61–68
7. Raeeszadeh-Sarmazdeh, M., Do, L. D., and Hritz, B. G. (2020) Metalloproteinases and their inhibitors: Potential for the development of new therapeutics. *Cells* **9**, 1313
8. Coussens, L. M., Fingleton, B., and Matrisian, L. M. (2002) Matrix metalloproteinase inhibitors and cancer: Trials and tribulations. *Science* **295**, 2387–2392
9. Martin, M. D., and Matrisian, L. M. (2007) The other side of MMPs: Protective roles in tumor progression. *Cancer Metastasis Rev.* **26**, 717–724
10. Decock, J., Thirkettle, S., Wagstaff, L., and Edwards, D. R. (2011) Matrix metalloproteinases: Protective roles in cancer. *J. Cell. Mol. Med.* **15**, 1254–1265
11. Overall, C. M., and Kleinfeld, O. (2006) Tumour microenvironment - opinion: Validating matrix metalloproteinases as drug targets and anti-targets for cancer therapy. *Nat. Rev. Cancer* **6**, 227–239
12. Wang, Y., Xue, P., Cao, M., Yu, T., Lane, S. T., and Zhao, H. (2021) Directed evolution: Methodologies and applications. *Chem. Rev.* **121**, 12384–12444

13. Könnig, D., and Kolmar, H. (2018) Beyond antibody engineering: Directed evolution of alternative binding scaffolds and enzymes using yeast surface display. *Microb. Cell Fact.* **17**, 32
14. Batra, J., and Radisky, E. S. (2014) Tissue inhibitors of metalloproteinases (TIMPs): Inhibition of Zn-dependent metalloproteinases. In: Scott, R. A., ed. *Encyclopedia of Inorganic and Bioinorganic Chemistry*, John Wiley & Sons, Chichester: 1–10
15. Huang, W., Suzuki, K., Nagase, H., Arumugam, S., Van Doren, S. R., and Brew, K. (1996) Folding and characterization of the amino-terminal domain of human tissue inhibitor of metalloproteinases-1 (TIMP-1) expressed at high yield in *E. coli*. *FEBS Lett.* **384**, 155–161
16. Murphy, G., Houbrechts, A., Cockett, M. I., Williamson, R. A., O'Shea, M., and Docherty, A. J. (1991) The N-terminal domain of tissue inhibitor of metalloproteinases retains metalloproteinase inhibitory activity. *Biochemistry* **30**, 8097–8102
17. Arkadash, V., Yosef, G., Shirian, J., Cohen, I., Horev, Y., Grossman, M., Sagi, I., Radisky, E. S., Shifman, J. M., and Papo, N. (2017) Development of high affinity and high specificity inhibitors of matrix metalloproteinase 14 through computational design and directed evolution. *J. Biol. Chem.* **292**, 3481–3495
18. Shirian, J., Arkadash, V., Cohen, I., Sapir, T., Radisky, E. S., Papo, N., and Shifman, J. M. (2018) Converting a broad matrix metalloproteinase family inhibitor into a specific inhibitor of MMP-9 and MMP-14. *FEBS Lett.* **592**, 1122–1134
19. Yosef, G., Arkadash, V., and Papo, N. (2018) Targeting the MMP-14/MMP-2/integrin α v β 3 axis with multispecific N-TIMP2-based antagonists for cancer therapy. *J. Biol. Chem.* **293**, 13310–13326
20. Arkadash, V., Radisky, E. S., and Papo, N. (2018) Combinatorial engineering of N-TIMP2 variants that selectively inhibit MMP9 and MMP14 function in the cell. *Oncotarget* **9**, 32036–32053
21. Raezadeh-Sarmazdeh, M., Greene, K. A., Sankaran, B., Downey, G. P., Radisky, D. C., and Radisky, E. S. (2019) Directed evolution of the metalloproteinase inhibitor TIMP-1 reveals that its N- and C-terminal domains cooperate in matrix metalloproteinase recognition. *J. Biol. Chem.* **294**, 9476–9488
22. Batra, J., Robinson, J., Soares, A. S., Fields, A. P., Radisky, D. C., and Radisky, E. S. (2012) Matrix metalloproteinase-10 (MMP-10) interaction with tissue inhibitors of metalloproteinases TIMP-1 and TIMP-2: Binding studies and crystal structure. *J. Biol. Chem.* **287**, 15935–15946
23. Batra, J., Soares, A. S., Mehner, C., and Radisky, E. S. (2013) Matrix metalloproteinase-10/TIMP-2 structure and analyses define conserved core interactions and diverse exosite interactions in MMP/TIMP complexes. *PLoS One* **8**, e75836
24. Sternlicht, M. D., Bissell, M. J., and Werb, Z. (2000) The matrix metalloproteinase stromelysin-1 acts as a natural mammary tumor promoter. *Oncogene* **19**, 1102–1113
25. Sternlicht, M. D., Lochter, A., Sympon, C. J., Huey, B., Rougier, J. P., Gray, J. W., Pinkel, D., Bissell, M. J., and Werb, Z. (1999) The stromal proteinase MMP3/stromelysin-1 promotes mammary carcinogenesis. *Cell* **98**, 137–146
26. Radisky, D. C., Levy, D. D., Littlepage, L. E., Liu, H., Nelson, C. M., Fata, J. E., Leake, D., Godden, E. L., Albertson, D. G., Nieto, M. A., Werb, Z., and Bissell, M. J. (2005) Rac1b and reactive oxygen species mediate MMP-3-induced EMT and genomic instability. *Nature* **436**, 123–127
27. Stallings-Mann, M. L., Waldmann, J., Zhang, Y., Miller, E., Gauthier, M. L., Visscher, D. W., Downey, G. P., Radisky, E. S., Fields, A. P., and Radisky, D. C. (2012) Matrix metalloproteinase induction of Rac1b, a key effector of lung cancer progression. *Sci. Transl. Med.* **4**, 142ra195
28. Mehner, C., Miller, E., Khau, D., Nassar, A., Oberg, A. L., Bamlet, W. R., Zhang, L., Waldmann, J., Radisky, E. S., and Crawford, H. C. (2014) Tumor cell-derived MMP3 Orchestrates Rac1b and tissue alterations that promote pancreatic adenocarcinoma. *Mol. Cancer Res.* **12**, 1430–1439
29. Green, M., Gough, A., Devlin, J., Smith, J., Astin, P., Taylor, D., and Emery, P. (2003) Serum MMP-3 and MMP-1 and progression of joint damage in early rheumatoid arthritis. *Rheumatology* **42**, 83–88
30. Yamashita, C. M., Cybulskie, C., Milos, S., Zuo, Y. Y., McCaig, L. A., and Veldhuizen, R. A. (2016) The effect of matrix metalloproteinase-3 deficiency on pulmonary surfactant in a mouse model of acute lung injury. *Can. J. Physiol. Pharmacol.* **94**, 682–685
31. Yamashita, C. M., Radisky, D. C., Aschner, Y., and Downey, G. P. (2014) The importance of matrix metalloproteinase-3 in respiratory disorders. *Expert Rev. Respir. Med.* **8**, 411–421
32. Yamashita, C. M., Dolgonos, L., Zemans, R. L., Young, S. K., Robertson, J., Briones, N., Suzuki, T., Campbell, M. N., Gaudie, J., Radisky, D. C., Riches, D. W., Yu, G., Kaminski, N., McCulloch, C. A., and Downey, G. P. (2011) Matrix metalloproteinase 3 is a mediator of pulmonary fibrosis. *Am. J. Pathol.* **179**, 1733–1745
33. Warner, R. L., Beltran, L., Younkin, E. M., Lewis, C. S., Weiss, S. J., Varani, J., and Johnson, K. J. (2001) Role of stromelysin 1 and gelatinase B in experimental acute lung injury. *Am. J. Respir. Cell Mol. Biol.* **24**, 537–544
34. Nerusu, K. C., Warner, R. L., Bhagavathula, N., McClintock, S. D., Johnson, K. J., and Varani, J. (2007) Matrix metalloproteinase-3 (stromelysin-1) in acute inflammatory tissue injury. *Exp. Mol. Pathol.* **83**, 169–176
35. Fligel, S. E., Standiford, T., Fligel, H. M., Tashkin, D., Strieter, R. M., Warner, R. L., Johnson, K. J., and Varani, J. (2006) Matrix metalloproteinases and matrix metalloproteinase inhibitors in acute lung injury. *Hum. Pathol.* **37**, 422–430
36. Vandooren, J., Van den Steen, P. E., and Opdenakker, G. (2013) Biochemistry and molecular biology of gelatinase B or matrix metalloproteinase-9 (MMP-9): The next decade. *Crit. Rev. Biochem. Mol. Biol.* **48**, 222–272
37. Gomis-Ruth, F. X., Maskos, K., Betz, M., Bergner, A., Huber, R., Suzuki, K., Yoshida, N., Nagase, H., Brew, K., Bourenkov, G. P., Bartunik, H., and Bode, W. (1997) Mechanism of inhibition of the human matrix metalloproteinase stromelysin-1 by TIMP-1. *Nature* **389**, 77–81
38. Boder, E. T., Raezadeh-Sarmazdeh, M., and Price, J. V. (2012) Engineering antibodies by yeast display. *Arch. Biochem. Biophys.* **526**, 99–106
39. Boder, E. T., and Wittrup, K. D. (1997) Yeast surface display for screening combinatorial polypeptide libraries. *Nat. Biotechnol.* **15**, 553–557
40. Kuhlman, B., and Bradley, P. (2019) Advances in protein structure prediction and design. *Nat. Rev. Mol. Cell Biol.* **20**, 681–697
41. Fingleton, B. (2017) Matrix metalloproteinases as regulators of inflammatory processes. *Biochim. Biophys. Acta Mol. Cell Res.* **1864**, 2036–2042
42. Burrage, P. S., and Brinckerhoff, C. E. (2007) Molecular targets in osteoarthritis: Metalloproteinases and their inhibitors. *Curr. Drug Targets* **8**, 293–303
43. Razai, A. S., Eckelman, B. P., and Salvesen, G. S. (2020) Selective inhibition of matrix metalloproteinase 10 (MMP10) with a single-domain antibody. *J. Biol. Chem.* **295**, 2464–2472
44. Nam, D. H., Rodriguez, C., Remacle, A. G., Strongin, A. Y., and Ge, X. (2016) Active-site MMP-selective antibody inhibitors discovered from convex paratope synthetic libraries. *Proc. Natl. Acad. Sci. U. S. A.* **113**, 14970–14975
45. Artham, S., Verma, A., Newsome, A. S., and Somanath, P. R. (2020) Patients with acute respiratory distress syndrome exhibit increased stromelysin1 activity in the blood samples. *Cytokine* **131**, 155086
46. Artham, S., Gao, F., Verma, A., Alwhaibi, A., Sabbineni, H., Hafez, S., Ergul, A., and Somanath, P. R. (2019) Endothelial stromelysin1 regulation by the forkhead box-O transcription factors is crucial in the exudative phase of acute lung injury. *Pharmacol. Res.* **141**, 249–263
47. Puntorieri, V., McCaig, L. A., Howlett, C. J., Yao, L.-J., Lewis, J. F., Yamashita, C. M., and Veldhuizen, R. A. (2016) Lack of matrix metalloproteinase 3 in mouse models of lung injury ameliorates the pulmonary inflammatory response in female but not in male mice. *Exp. Lung Res.* **42**, 365–379
48. McMahan, R. S., Birkland, T. P., Smigiel, K. S., Vandivort, T. C., Rohani, M. G., Manicone, A. M., McGuire, J. K., Gharib, S. A., and Parks, W. C. (2016) Stromelysin-2 (MMP10) moderates inflammation by controlling macrophage activation. *J. Immunol.* **197**, 899–909
49. Kassim, S. Y., Gharib, S. A., Mecham, B. H., Birkland, T. P., Parks, W. C., and McGuire, J. K. (2007) Individual matrix metalloproteinases control distinct transcriptional responses in airway epithelial cells infected with *Pseudomonas aeruginosa*. *Infect. Immun.* **75**, 5640–5650

50. Vandivort, T. C., Birkland, T. P., Domiciano, T. P., Mitra, S., Kavanagh, T. J., and Parks, W. C. (2017) Stromelysin-2 (MMP-10) facilitates clearance and moderates inflammation and cell death following lung exposure to long multiwalled carbon nanotubes. *Int. J. Nanomedicine* **12**, 1019
51. Craig, V. J., Zhang, L., Hagood, J. S., and Owen, C. A. (2015) Matrix metalloproteinases as therapeutic targets for idiopathic pulmonary fibrosis. *Am. J. Respir. Cell Mol. Biol.* **53**, 585–600
52. Albaiceta, G. M., Gutiérrez-Fernández, A., Parra, D., Astudillo, A., García-Prieto, E., Taboada, F., and Fueyo, A. (2008) Lack of matrix metalloproteinase-9 worsens ventilator-induced lung injury. *Am. J. Physiol. Lung Cell Mol. Physiol.* **294**, L535–L543
53. Yoon, H.-K., Cho, H.-Y., and Kleberger, S. R. (2007) Protective role of matrix metalloproteinase-9 in ozone-induced airway inflammation. *Environ. Health Perspect.* **115**, 1557–1563
54. Yu, G., Kovkarova-Naumovski, E., Jara, P., Parwani, A., Kass, D., Ruiz, V., Lopez-Otín, C., Rosas, I. O., Gibson, K. F., and Cabrera, S. (2012) Matrix metalloproteinase-19 is a key regulator of lung fibrosis in mice and humans. *Am. J. Respir. Crit. Care Med.* **186**, 752–762
55. Sen, A. I., Shiomi, T., Okada, Y., and D'Armiento, J. M. (2010) Deficiency of matrix metalloproteinase-13 increases inflammation after acute lung injury. *Exp. Lung Res.* **36**, 615–624
56. Nkyimbeng, T., Ruppert, C., Shiomi, T., Dahal, B., Lang, G., Seeger, W., Okada, Y., D'Armiento, J., and Günther, A. (2013) Pivotal role of matrix metalloproteinase 13 in extracellular matrix turnover in idiopathic pulmonary fibrosis. *PLoS One* **8**, e73279
57. Cabrera, S., Maciel, M., Hernández-Barrientos, D., Calyeca, J., Gaxiola, M., Selman, M., and Pardo, A. (2019) Delayed resolution of bleomycin-induced pulmonary fibrosis in absence of MMP13 (collagenase 3). *Am. J. Physiol. Lung Cell Mol. Physiol.* **316**, L961–L976
58. Manicone, A. M., Birkland, T. P., Lin, M., Betsuyaku, T., Van Rooijen, N., Lohi, J., Keski-Oja, J., Wang, Y., Skerrett, S. J., and Parks, W. C. (2009) Epilysin (MMP-28) restrains early macrophage recruitment in *Pseudomonas aeruginosa* pneumonia. *J. Immunol.* **182**, 3866–3876
59. Mata-Fink, J., Kriegsman, B., Yu, H. X., Zhu, H., Hanson, M. C., Irvine, D. J., and Wittrup, K. D. (2013) Rapid conformational epitope mapping of anti-gp120 antibodies with a designed mutant panel displayed on yeast. *J. Mol. Biol.* **425**, 444–456
60. Suzuki, K., Kan, C. C., Hung, W., Gehring, M. R., Brew, K., and Nagase, H. (1998) Expression of human pro-matrix metalloproteinase 3 that lacks the N-terminal 34 residues in *Escherichia coli*: Autoactivation and interaction with tissue inhibitor of metalloproteinase 1 (TIMP-1). *Biol. Chem.* **379**, 185–191
61. Marcy, A. L., Eiberger, L. L., Harrison, R., Chan, H. K., Hutchinson, N. I., Hagmann, W. K., Cameron, P. M., Boulton, D. A., and Hermes, J. D. (1991) Human fibroblast stromelysin catalytic domain: Expression, purification, and characterization of a C-terminally truncated form. *Biochemistry* **30**, 6476–6483
62. Suzuki, K., Enghild, J. J., Morodomi, T., Salvesen, G., and Nagase, H. (1990) Mechanisms of activation of tissue procollagenase by matrix metalloproteinase 3 (stromelysin). *Biochemistry* **29**, 10261–10270
63. Nagase, H., Enghild, J. J., Suzuki, K., and Salvesen, G. (1990) Stepwise activation mechanisms of the precursor of matrix metalloproteinase 3 (stromelysin) by proteinases and (4-aminophenyl)mercuric acetate. *Biochemistry* **29**, 5783–5789
64. Elkins, P. A., Ho, Y. S., Smith, W. W., Janson, C. A., D'Alessio, K. J., McQueney, M. S., Cummings, M. D., and Romanic, A. M. (2002) Structure of the C-terminally truncated human ProMMP9, a gelatin-binding matrix metalloproteinase. *Acta Crystallogr. D Biol. Crystallogr.* **58**, 1182–1192
65. Crombez, L., Marques, B., Lenormand, J. L., Mouz, N., Polack, B., Trocme, C., and Toussaint, B. (2005) High level production of secreted proteins: Example of the human tissue inhibitor of metalloproteinases 1. *Biochem. Biophys. Res. Commun.* **337**, 908–915
66. Morrison, J. F. (1969) Kinetics of the reversible inhibition of enzyme-catalysed reactions by tight-binding inhibitors. *Biochim. Biophys. Acta* **185**, 269–286
67. McPherson, A., and Cudney, B. (2014) Optimization of crystallization conditions for biological macromolecules. *Acta Crystallogr. F Struct. Biol. Commun.* **70**, 1445–1467
68. Batty, T. G., Kontogiannis, L., Johnson, O., Powell, H. R., and Leslie, A. G. (2011) iMOSFLM: A new graphical interface for diffraction-image processing with MOSFLM. *Acta Crystallogr. D Biol. Crystallogr.* **67**, 271–281
69. Evans, P. (2006) Scaling and assessment of data quality. *Acta Crystallogr. D Biol. Crystallogr.* **62**, 72–82
70. Evans, P. R., and Murshudov, G. N. (2013) How good are my data and what is the resolution? *Acta Crystallogr. D Biol. Crystallogr.* **69**, 1204–1214
71. Vagin, A., and Teplyakov, A. (2010) Molecular replacement with MOLREP. *Acta Crystallogr. D Biol. Crystallogr.* **66**, 22–25
72. McCoy, A. J. (2007) Solving structures of protein complexes by molecular replacement with Phaser. *Acta Crystallogr. D Biol. Crystallogr.* **63**, 32–41
73. McCoy, A. J., Grosse-Kunstleve, R. W., Adams, P. D., Winn, M. D., Storoni, L. C., and Read, R. J. (2007) Phaser crystallographic software. *J. Appl. Crystallogr.* **40**, 658–674
74. Afonine, P. V., Grosse-Kunstleve, R. W., and Adams, P. D. (2005) The Phenix refinement framework. *CCP4 Newsl.* **42**, 42
75. Emsley, P., and Cowtan, K. (2004) Coot: Model-building tools for molecular graphics. *Acta Crystallogr. D Biol. Crystallogr.* **60**, 2126–2132
76. Painter, J., and Merritt, E. A. (2006) Optimal description of a protein structure in terms of multiple groups undergoing TLS motion. *Acta Crystallogr. D Biol. Crystallogr.* **62**, 439–450
77. Kayode, O., Wang, R., Pendlebury, D. F., Cohen, I., Henin, R. D., Hockla, A., Soares, A. S., Papo, N., Caulfield, T. R., and Radisky, E. S. (2016) An acrobatic substrate metamorphosis reveals a requirement for substrate conformational dynamics in trypsin proteolysis. *J. Biol. Chem.* **291**, 26304–26319
78. Cohen, I., Coban, M., Shahar, A., Sankaran, B., Hockla, A., Lacham, S., Caulfield, T. R., Radisky, E. S., and Papo, N. (2019) Disulfide engineering of human Kunitz-type serine protease inhibitors enhances proteolytic stability and target affinity toward mesotrypsin. *J. Biol. Chem.* **294**, 5105–5120
79. Coban, M. A., Morrison, J., Maharjan, S., Hernandez Medina, D. H., Li, W., Zhang, Y. S., Freeman, W. D., Radisky, E. S., Le Roch, K. G., Weisend, C. M., Ebihara, H., and Caulfield, T. R. (2021) Attacking COVID-19 progression using multi-drug therapy for synergetic target engagement. *Biomolecules* **11**, 787
80. Krieger, E., Koraimann, G., and Vriend, G. (2002) Increasing the precision of comparative models with YASARA NOVA—a self-parameterizing force field. *Proteins* **47**, 393–402